

MORPHOLOGICAL AND KINEMATIC EVOLUTION OF THREE INTERACTING CORONAL MASS EJECTIONS OF 2011 FEBRUARY 13–15

WAGEESH MISHRA AND NANDITA SRIVASTAVA

Udaipur Solar Observatory, Physical Research Laboratory, P.O. Box 198, Badi Road, Udaipur 313001, India; wageesh@prl.res.in

Received 2014 February 28; accepted 2014 August 18; published 2014 September 24

ABSTRACT

During 2011 February 13–15, three Earth-directed coronal mass ejections (CMEs) launched in succession were recorded as limb CMEs by *STEREO*/SECCHI coronagraphs (COR). These CMEs provided an opportunity to study their geometrical and kinematic evolution from multiple vantage points. In this paper, we examine the differences in geometrical evolution of slow and fast CMEs during their propagation in the heliosphere. We also study their interaction and collision using *STEREO*/SECCHI COR and Heliospheric Imager (HI) observations. We have found evidence of interaction and collision between the CMEs of February 15 and 14 in the COR2 and HI1 field of view (FOV), respectively, while the CME of February 14 caught up with the CME of February 13 in the HI2 FOV. By estimating the true mass of these CMEs and using their pre- and post-collision dynamics, the momentum and energy exchange between them during the collision phase are studied. We classify the nature of the observed collision between the CMEs of February 14 and 15 as inelastic, reaching close to the elastic regime. Relating imaging observations with in situ *WIND* measurements at L1, we find that the CMEs move adjacent to each other after their collision in the heliosphere and are recognized as distinct structures in in situ observations. Our results highlight the significance of HI observations in studying CME–CME collision for the purpose of improved space weather forecasting.

Key words: shock waves – Sun: coronal mass ejections (CMEs) – Sun: heliosphere

Online-only material: color figures

1. INTRODUCTION

Coronal mass ejections (CMEs) are frequent expulsions of massive magnetized plasma from the solar corona into the heliosphere. If the CMEs are directed toward the Earth and have an enhanced southward magnetic field, they can result in severe geomagnetic storms (Dungey 1961; Gosling et al. 1990; Echer et al. 2008). The typical transit time of CMEs from the Sun to the Earth is between one and four days and the number of CMEs launched from the Sun is about three per day at maximum solar activity (St. Cyr et al. 2000). Therefore, the interaction of CMEs in the heliosphere is expected to be more frequent near solar maximum. The possibility of CME–CME interaction was reported early by analyzing in situ observations of CMEs by the *Pioneer 9* spacecraft (Intriligator 1976). Also, Burlaga et al. (1987) presented an additional case of CME–CME interaction in the heliosphere using in situ observations of the twin *Helios* spacecraft. They showed that compound streams are formed due to such interactions, which have amplified parameters responsible for producing major geomagnetic storms. Using the wide field-of-view (FOV) coronagraphic observations of Large Angle Spectrometric COronagraph (LASCO; Brueckner et al. 1995) on board the *SOlar and Heliospheric Observatory* (*SOHO*) and long-wavelength radio observations, Gopalswamy et al. (2001) provided the first evidence for CME–CME interaction. Burlaga et al. (2002) identified a set of successive halo CMEs directed toward the Earth and found that they appeared as complex ejecta near 1 AU (Burlaga et al. 2001). They inferred that these CMEs, launched successively, merged en route from the Sun to the Earth and formed complex ejecta in which the identity of individual CMEs was lost.

CME–CME interactions are also important as they can result in an extended period of an enhanced southward magnetic field, which can cause intense geomagnetic storms (Farrugia & Berdichevsky 2004; Farrugia et al. 2006). They help to under-

stand the collisions between large-scale magnetized plasmoids and hence the various plasma processes involved. Also, if a shock from a following CME penetrates a preceding CME, it provides a unique opportunity to study the evolution of the shock strength and structure and its effect on preceding CME plasma parameters (Lugaz et al. 2005; Möstl et al. 2012; Liu et al. 2012). Since, estimating the arrival time of CMEs at the Earth is crucial for predicting space weather effects near the Earth and CME–CME interactions are responsible for changing the dynamics of interacting CMEs in the heliosphere, such interactions need to be examined in detail. Furthermore, reconnection between magnetic flux ropes of CMEs can be explored by studying cases of CME–CME interactions (Gopalswamy et al. 2001; Wang et al. 2003) that are also known to lead to solar energetic particle (SEP) events (Gopalswamy et al. 2002).

Prior to the launch of the *Solar TErrestrial RElations Observatory* (*STEREO*; Kaiser et al. 2008), CME interaction study was limited to analyzing imaging observations near the Sun, in situ observations near the Earth, and simulation studies (Vandas et al. 1997; Odstrcil et al. 2003; Lugaz et al. 2005). Since the launch of *STEREO* in 2006, its Sun Earth Connection Coronal and Heliospheric Investigation (SECCHI; Howard et al. 2008) package, which consists of remote sensing instruments, has been capable of imaging a CME from its lift-off in the corona up to the Earth and beyond. It also enables us to witness CME–CME interaction in the heliosphere. Using Heliospheric Imager (HI) observations, studies of CME interaction have increased significantly, e.g., the interacting CMEs of 2008 November 2 (Shen et al. 2012) and of 2010 May 23–24 (Lugaz et al. 2012), and the extensively studied CMEs of 2010 August 1 (Harrison et al. 2012; Liu et al. 2012; Möstl et al. 2012; Temmer et al. 2012).

In the present work, we have selected three Earth-directed interacting CMEs launched during 2011 February 13–15 from NOAA AR 11158 when the twin *STEREO* spacecraft were separated by approximately 180°. The interaction of these CMEs

has been studied based on imaging and in situ observations from the *STEREO* and *WIND* spacecraft, respectively. Such a study is required to improve our understanding about the nature and consequences of interaction. These interacting CMEs have also been studied earlier, e.g., by Marićić et al. (2014) and Temmer et al. (2014).

Marićić et al. (2014) used the plane of sky (POS) approximation and Harmonic Mean (HM) method (Lugaz et al. 2009) to convert the derived elongation-time profiles from the single *STEREO* spacecraft to distance–time profiles and then estimated the arrival time of CMEs at L1. Their approach seems to be less reliable at larger elongation where the direction of propagation and structure of CME play a crucial role. Further, Marićić et al. (2014) could track a CME feature only up to small elongations ($\approx 25^\circ$). However, in our analysis we have constructed *J*-maps (Sheeley et al. 1999; Davies et al. 2009) that allow us to follow the CMEs to significantly greater elongations ($\approx 45^\circ$). Previous studies have shown that the tracking of CMEs to larger elongation using *J*-maps and subsequent stereoscopic reconstruction give more precise kinematics and estimates of the arrival time of CMEs than employing single spacecraft reconstruction methods (Williams et al. 2009; Liu et al. 2010a; Lugaz 2010; Mishra & Srivastava 2013; Colaninno et al. 2013; Mishra et al. 2014b). In our study, we have applied the stereoscopic methods (SSSE; Davies et al. 2013, TAS; Lugaz et al. 2010; and GT, Liu et al. 2010a), which apart from dynamics also yield the time variations of direction of propagation of CMEs. Lugaz et al. (2012) have found a change in the longitudinal direction of the propagation of CMEs during their interaction. Such a deflection is of prime concern for predicting CME arrival time at Earth and to understand the collision dynamics of CMEs, which are the main objectives of the present paper. We have estimated the kinematics of overall CME structure using the Graduated Cylindrical Shell (GCS) model (Thernisien et al. 2009) in COR2 FOV while Marićić et al. (2014) estimated the kinematics of a single tracked feature. The kinematics of overall CME structure in COR2 FOV is helpful for determining the probability of collision of CMEs beyond COR2 FOV. Temmer et al. (2014) studied the interaction of February 14–15 CMEs corresponding to different position angles measured over the entire latitudinal extent of these CMEs. In this context, the present study is important as it also focuses on understanding the nature of collision by estimating momentum and energy exchange during the collision phase of the CMEs.

The unique positioning of the *STEREO* spacecraft, from the time of its launch, enticed us to perform an additional study about the geometrical evolution of these Earth-directed CMEs in COR2 FOV from identical multiple viewpoints. The location of active regions (S20E04 to S20W12 during February 13–15) for these CMEs allowed its SECCHI/COR coronagraph to observe these Earth-directed CMEs at the limb (i.e., plane orthogonal to the Sun–*STEREO* line), contrary to *SOHO*/LASCO observations, which always record such CMEs as halos. In this scenario, the CME observations are least affected by the projection effects in both SECCHI/COR-A and B FOV and hence crucial parameters, i.e., widths, speeds, etc., that define the geo-effectiveness of CMEs can be determined with reasonable accuracy. Morphological studies have been carried out earlier, assuming either a cone or ice-cream-cone model for CMEs for estimating the true angular width, central position angle, radial speed, and acceleration of halo CMEs (Zhao et al. 2002; Michałek et al. 2003; Xie et al. 2004; Xue et al. 2005). Also, Howard et al. (1982), Fisher & Munro (1984) suggested

that the geometrical properties of CMEs can be described by a cone model, which can be used to estimate their mass. All the cone models assume that the angular width of CMEs remains constant beyond a few solar radii as they propagate through the solar corona. Vršnak et al. (2010, 2013) also assumed a constant cone angular width of a CME for developing the drag-based model (DBM) of the propagation of CMEs. Our study of the morphological evolution of the selected CMEs is expected to provide results that can help to refine the cone model by incorporating the possible variation in angular width of CMEs corresponding to their different speed, i.e., slower, comparable, and faster than the ambient solar wind speed.

In Section 2.1, we present the morphological evolution of CMEs. In Section 2.2, the kinematics and interaction of CMEs in the heliosphere are discussed. In Section 2.2.2, the angular widths of CMEs determined from two-dimensional (2D) images are compared with the angular widths derived from the GCS model. In Section 2.3, we focus on the nature of collision and estimate the energy and momentum transfer during collision of CMEs. In Section 3.1, in situ observations of CMEs are described. Sections 3.2 and 3.3 describe the arrival of CMEs at L1 and their geomagnetic response, respectively. The main results of the present study are discussed in Section 4.

2. REMOTE SENSING OBSERVATIONS AND ANALYSIS

In this section, we summarize the imaging observations of CMEs during 2011 February 13 to 15 taken by the *STEREO*/SECCHI package, which consists of five telescopes, namely one Extreme Ultraviolet Imager (EUVI), two coronagraphs (COR1 and COR2), and two Heliospheric Imagers (HI1 and HI2). Unlike COR, the HI camera is off-center from the Sun's center and can observe CMEs from the outer edge of FOV of COR2 up to the Earth and beyond (Eyles et al. 2009). At the time of observations of CMEs presented in this study, *STEREO*-A was $\approx 87^\circ$ West and *STEREO*-B was $\approx 94^\circ$ East of the Earth. They were approximately in the ecliptic plane at 0.96 AU and 1.0 AU distance from the Sun.

The CME of February 13 (hereinafter, CME1) was observed by *SOHO*/LASCO-C2 at 18:36 UT on 2011 February 13 as a faint partial halo CME with an angular width of 276° . In SECCHI/COR1-A and B, this CME appeared at 17:45 UT in the SE and SW quadrants, respectively. The CME of February 14 (hereinafter, CME2) was first recorded by *SOHO*/LASCO-C2 at 18:24 UT on 2011 February 14 as a halo CME. CME2 appeared in SECCHI/COR1-A and B at 17:45 UT at the east and west limbs, respectively. In *SOHO*/LASCO-C2 FOV, the CME of February 15 (hereinafter, CME3) was first observed at 02:24 UT on 2011 February 15 as a halo CME. In the SECCHI/COR1-A and B images, the CME3 was first observed at 02:05 UT at the east and west limbs, respectively.

2.1. Morphological Evolution of CMEs in the COR Field-of-view

We measured the geometrical properties (e.g., cone angle) of the selected CMEs by analyzing the SECCHI/COR2 images. Our aim is to study the deviation of CMEs from the ideal cone model for CMEs with different speeds. We based our analysis on the concept that slow and fast CMEs interact with solar wind differently and hence, deviation of each from the cone model might be different. In the present study, we did not use COR1 images, as near the Sun, within a few solar radii, magnetic forces are dominant and also, CMEs are not fully developed.

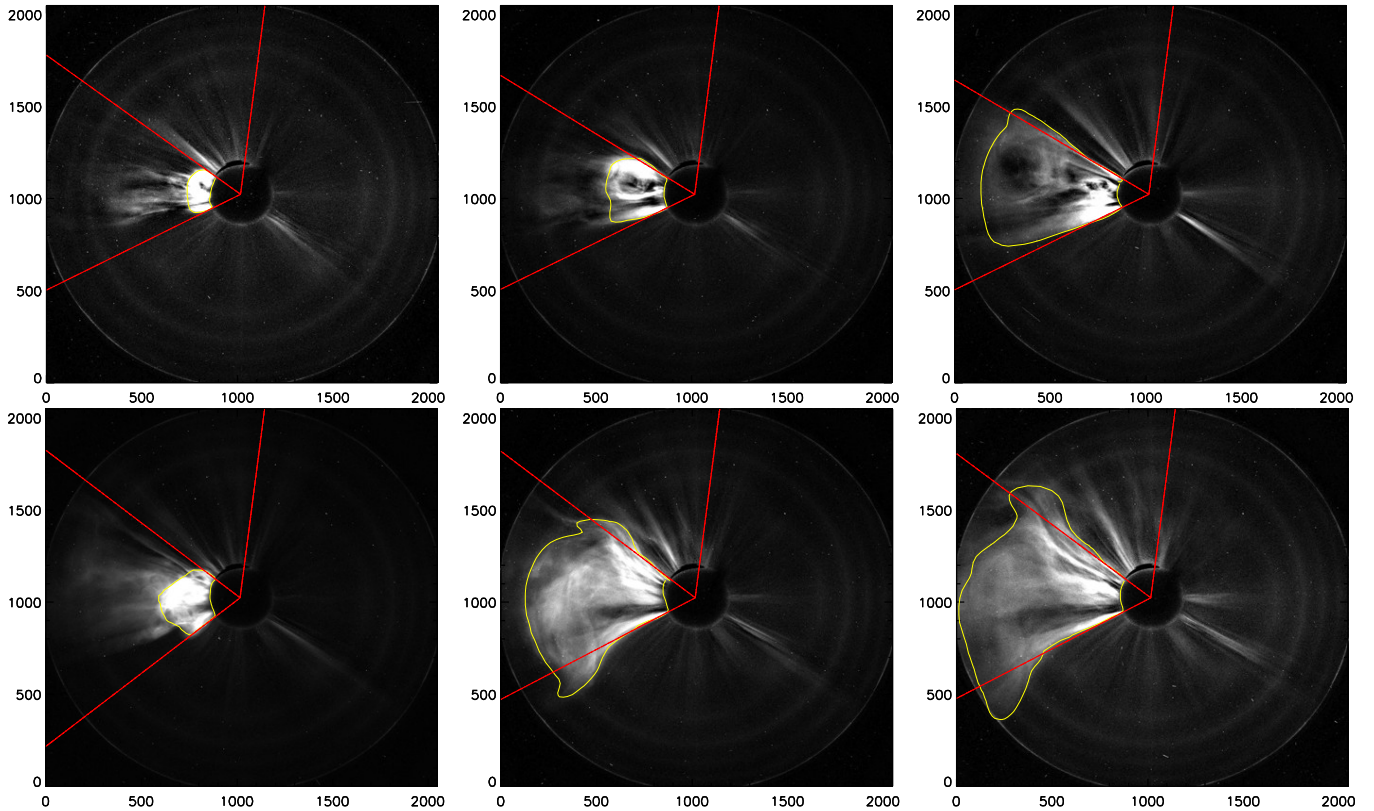


Figure 1. Left, middle, and right images in the top panel show CME2 in COR2-A FOV at 18:24 UT, 20:24 UT, and 23:54 UT on February 14, respectively. Similarly, left, middle, and right images in the bottom panel show CME3 in COR2-A FOV at 02:39 UT, 04:24 UT, and 05:54 UT on February 15, respectively. The vertical red lines mark the zero degree position angle in helio-projective radial coordinate system. The other two red lines forming the edges of the CME cone are marked at the position angle of the CME flanks. The contour with the yellow curve encloses the CME area completely.

(A color version of this figure is available in the online journal.)

We excluded the CME1 for morphological study because it was very faint in COR2 FOV. We selected CME2 and CME3 for the morphological analysis that had different speeds in COR2 FOV.

We began with the ice-cream-cone model of Xue et al. (2005), which considers the shape of CMEs to be a symmetrical cone combined with a sphere. As per this model, the apex of the cone and the center of the sphere are both located at the center of the Sun and CMEs move radially outward, having a constant cone angular width beyond a few solar radii from the Sun. We measured the cone angular width of CMEs using COR2 images and estimated the cone area, i.e., $A = \pi r^2 \Theta / 360$, where Θ is the cone angular width in degrees and r is the radius of the sphere, which is equal to the distance between the front edge of the CME and the center of the Sun. For the estimation of r and Θ , we avoided the use of coordinate conversion as we deal with CMEs approximately perpendicular to the camera of the *STEREO* spacecraft. Hence, the estimated area using the above equation is the area of the CME as it appears from the side (perpendicular to its motion).

In order to calculate the cone area as described above, we processed the SECCHI/COR2 images of CME2 and CME3 and then subtracted a background image from them. Furthermore, we enclosed the CME area by manual clicking and joining the points on the CME boundary. We also used a few initial points on each side of the CME flank close to the coronagraph occulter to get a cone model fit for each structure. These points were used to estimate the position angle at both flanks (near the apex of the cone) of the CMEs. The dif-

ference in position angle at both flanks is the 2D angular width of the CME. In the top panel of Figure 1, the evolution of the slow CME2 as observed in COR2-A images is shown with an overlaid contour enclosing the entire CME and overplotted lines denote the limiting position angle at both flanks of the CME. We repeated this analysis for the fast CME3, and its appearance in COR2-A FOV is shown in the bottom panel of Figure 1.

The estimated 2D cone angular width for CME2 and CME3 in COR2 FOV is shown in Figure 2. From the figure, it is evident that the slow CME2 has a nearly constant (between 60° to 57°) 2D angular width in the COR2 FOV. For the fast CME3, its 2D angular width was $\approx 80^\circ$ in the beginning, which then decreased to 62° as it crossed the outer edge of COR2 FOV. From the contour in Figure 1 (top panel), it can be seen that CME2 followed the cone model and a slight spill of CME2 on the upper edge is compensated by a gap with the lower edge. For the fast CME3 (bottom panel of Figure 1), we noticed a significant spill on both sides (upper and lower edge) that increased with time in COR2-A FOV. The appearance and the variations of angular width of CME2 and CME3 in COR2-B images are the same as in COR2-A.

To calculate the ice-cream-cone model area (cone area) for both CMEs, we marked a point along the leading edge on each image, the distance of which from the center of the Sun gave the radius of the sphere located on the cone like a CME. Since some part of the CME is blocked by the occulter in all the images, the area of the CME blocked by the occulter has been subtracted from the sector (cone) area in order to compare it with the actual contour area of the CME. We

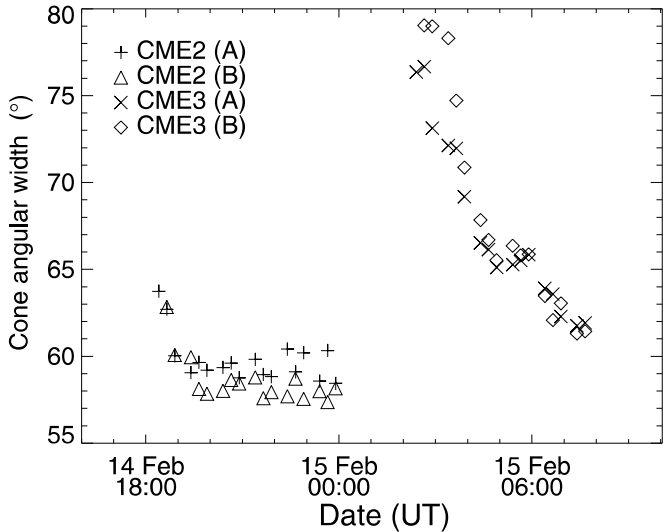


Figure 2. Time variation of the estimated 2D cone angular width of CME2 and CME3 from both COR-A and COR-B images.

also calculated the actual area enclosed by the CME contour (contour area). For convenience, both cone and contour areas have been measured in units of pixel². This is not of much

concern as it is the difference in the actual and the sector area we are interested in. In the top panels of Figures 3 and 4, the blue curves represent the cone area (i.e., the area obtained by approximating the CME with a cone model) and the red curves represent the actual contour area. From these figures, we note that for both CME2 and CME3, the time-variation of the cone and contour area shows a parabolic pattern in COR2-A and B FOV, which implies that A is proportional to r^2 . Therefore, we consider both fast and slow CMEs to follow the cone model to a certain extent.

From the top panel of Figure 3, we find that the cone area is larger than the contour area and both increased with time. In the bottom panels, we see that the difference in cone area and contour area is positive and increases as the CME2 propagates in the outer corona. For CME3, we can see (in the top panel of Figure 4) that the curves representing the cone and contour area intersect one another in both COR2-A and B FOV. In the bottom panels of this figure, the difference in cone and contour area decreases from positive (2.8×10^4 pixel² in COR2-A and 2.4×10^4 pixel² in COR2-B) to negative (-2.4×10^4 pixel² in COR2-A and -3.9×10^4 pixel² in COR2-B) as the CME3 propagates through the outer corona. This suggests that, at a certain height during its propagation in COR2 FOV, the contour area becomes larger than the estimated cone area. These findings indicate dissimilar morphological evolution for slow and fast CMEs in the corona.

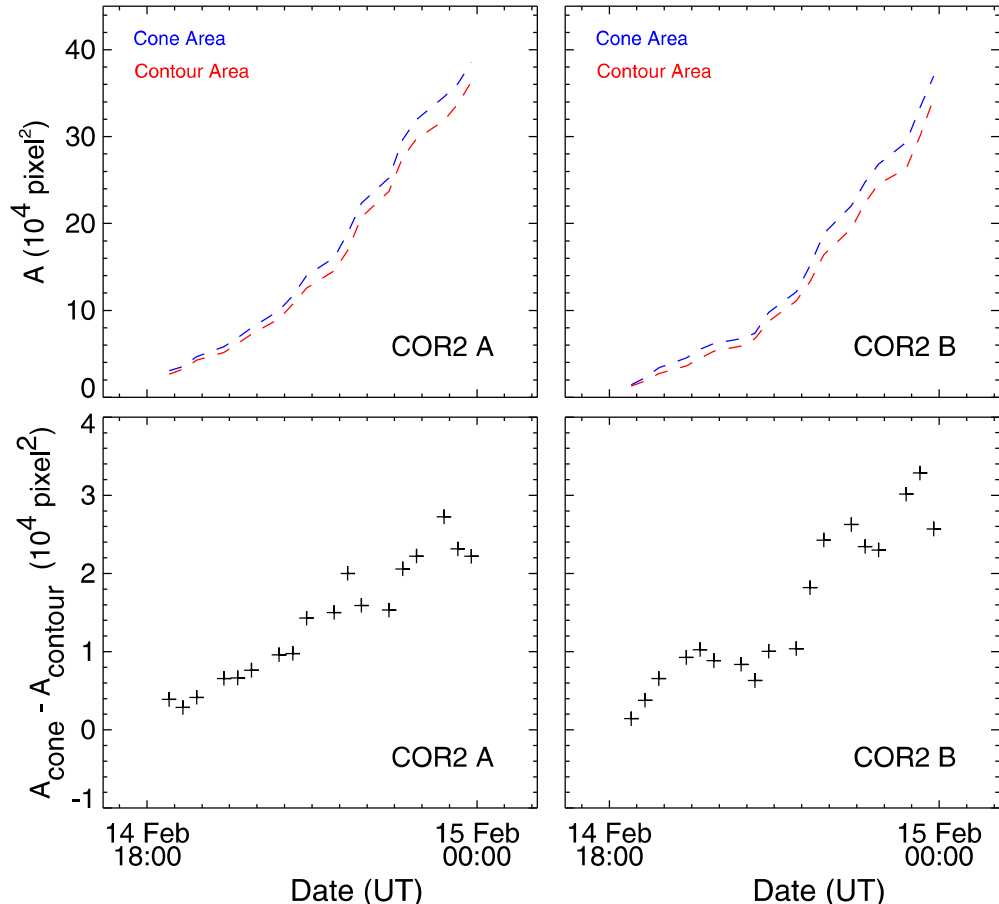


Figure 3. In the top left panel, time variations in the cone and contour area of CME2 estimated in COR2-A FOV is shown with blue and red, respectively. Its variations in COR2-B FOV are shown in top right panel. In the bottom left and right panels, the difference in cone and contour area, estimated for COR2-A and B FOV, respectively, are shown.

(A color version of this figure is available in the online journal.)

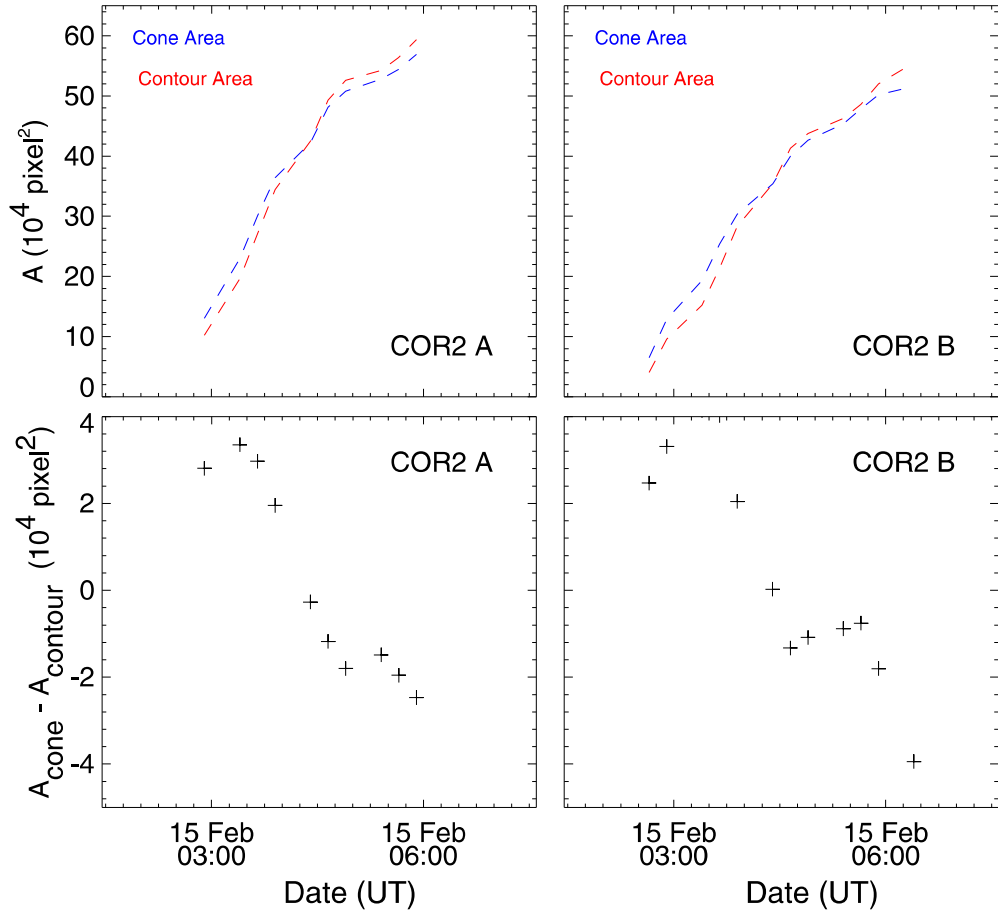


Figure 4. As Figure 3, for the CME3.
(A color version of this figure is available in the online journal.)

2.2. Kinematic Evolution and Interaction of CMEs in the Heliosphere

2.2.1. 3D Reconstruction in COR2 Field of View

The launch of CME1, CME2, and CME3 from the same active region in quick succession indicates the possibility of their interaction as they move out from the Sun into the heliosphere. To estimate the true kinematics of these CMEs, we have carried out the 3D reconstruction of CMEs using the GCS model developed by Thernisien et al. (2009). We apply the GCS model to contemporaneous images from SECCHI/COR2-B, SOHO/LASCO and SECCHI/COR2-A. Before applying the model, the total brightness images were processed and then a pre-event image was subtracted from a sequence of images to which the GCS model was applied. The images of CME1, CME2, and CME3 overlaid with the fitted GCS wireframed contour (hollow croissant) are shown in Figure 5.

The true kinematics estimated for these CMEs in COR2 FOV are shown in Figure 6. Because the CME1 was faint and non-structured, GCS model fitting could be done only for three consecutive images in COR2 FOV. The estimated longitudes (ϕ) for CME1, CME2, and CME3 at their last estimated height of $8.2 R_{\odot}$, $10.1 R_{\odot}$, and $11.1 R_{\odot}$ are -2° , 6° , and -3° , respectively. The estimated latitudes (θ) at these heights are -6° , 4° , and -11° for CME1, CME2, and CME3, respectively. The estimated 3D speed at their last estimated heights for CME1 (February 13, 20:54 UT), CME2 (February 14, 22:24 UT), and CME3 (February 15, 03:54 UT) is found

to be 618 km s^{-1} , 418 km s^{-1} , and 581 km s^{-1} , respectively. From the kinematics plot (Figure 6), it is clear that CME3 was faster than the preceding CME2 and headed approximately in the same direction toward the Earth. Moreover, the launch of CME3 preceded that of CME2 by ≈ 9 hr, and therefore, it is expected that these CMEs would interact at a certain distance in the heliosphere. Since the direction of propagation of CME1 and CME2 was also the same, there exists a possibility of interaction between CME1 and CME2 in the case that CME1 decelerates and CME2 accelerates beyond the estimated height in COR2 FOV. From the 3D reconstruction in COR2 FOV, we found that the speed of CME3 decreased very quickly from 1100 km s^{-1} at $6 R_{\odot}$ to 580 km s^{-1} at $11 R_{\odot}$ during 02:39 UT to 03:54 UT on 2011 February 15. A quick deceleration of the fast CME3 within 1.5 hr is most likely due to the interaction between CME2 and CME3. The terminology “interaction” and “collision” as used in this paper stand for two different senses. By “interaction,” we mean that one CME causes deceleration or acceleration of another, although no obvious signature of merging of propagation tracks of features corresponding to the two CMEs is noticed in the J -maps. The “collision” here is referred to as the phase during which the tracked features of two CMEs moving with different speeds come in close contact with each other until they achieve an approximately equal speed or their trend of acceleration is reversed or they get separated from each other. The fast deceleration of CME3 from the beginning of the COR2 FOV may occur due to various possibilities. It may be either due to the presence of dense material in the preceding

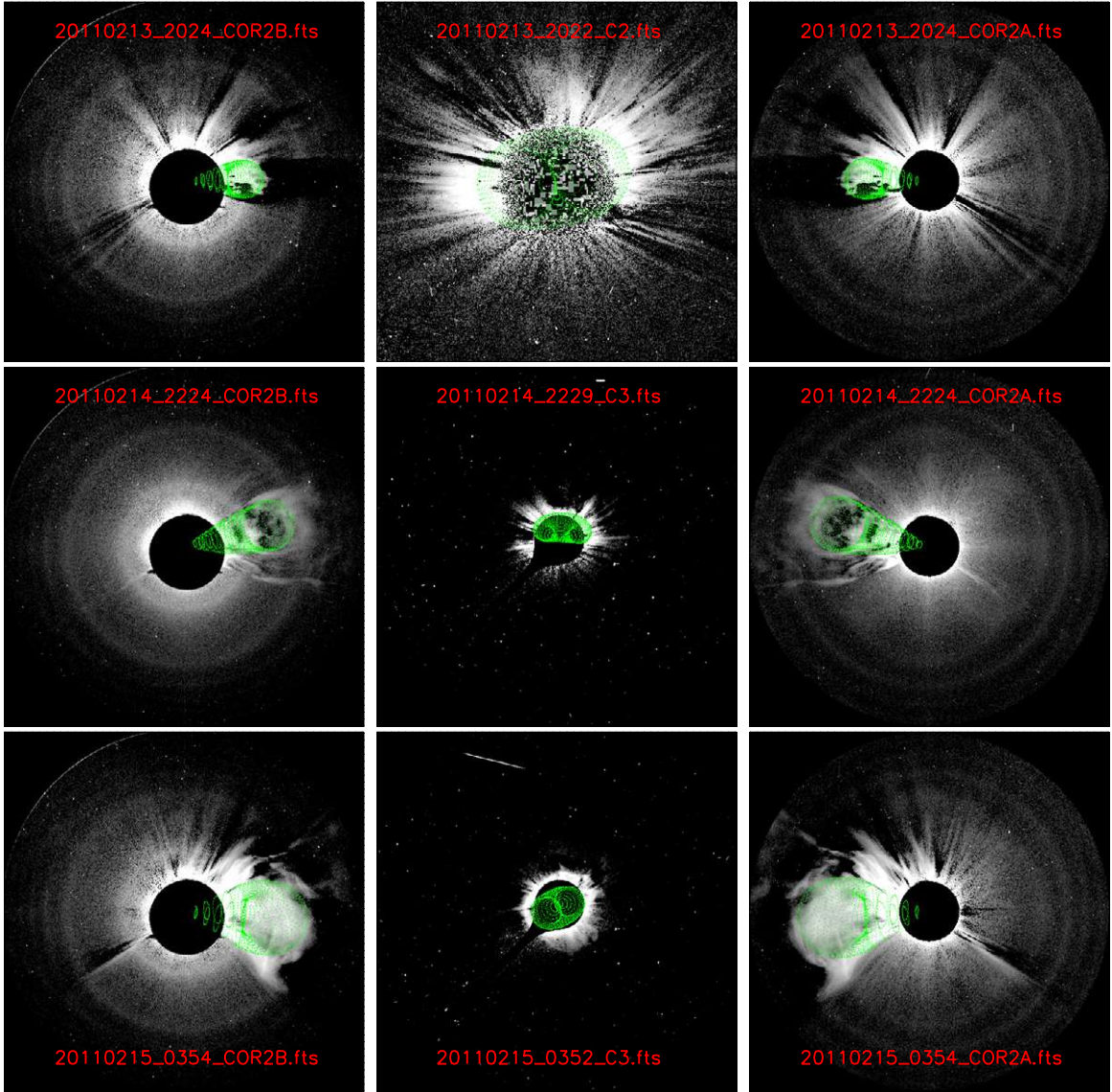


Figure 5. Contemporaneous image triplets for CMEs from SECCHI/COR2-B (left), *SOHO*/LASCO (C2 or C3) (middle) and SECCHI/COR2-A (right) are shown with GCS wireframe (with green) overlaid on it. The top, middle, and bottom panels show the images of CME1 around 20:24 UT on February 13, CME2 around 22:24 UT on February 14, and CME3 around 03:54 UT on February 15.

(A color version of this figure is available in the online journal.)

CME2 or due to the decrease of the magnetic driving forces of CME3 or due to the overlying curved magnetic field lines of the preceding CME2, which can act as a magnetic barrier for CME3 (Temmer et al. 2008, 2010, 2012).

2.2.2. Comparison of Angular Widths of CMEs Derived from the GCS Model

As discussed in Section 2.1, we have estimated the cone angular width of CMEs using 2D COR2 images, and it appears relevant to compare this to the angular width determined from the GCS model of 3D reconstruction. Using the GCS 3D reconstruction technique, apart from the kinematics of CMEs (explained in Section 2.2.1), we obtained the aspect ratios (κ) of the GCS model for CME1, CME2, and CME3 as 0.25, 0.28, and 0.37, respectively, at the last point of estimated distance in COR2 FOV. Also, we found the tilt angle (γ) around the axis of symmetry of the model to be 7° , -8° , and 25° for CME1, CME2, and CME3, respectively. The positive (negative)

value of the tilt shows that the rotation is counterclockwise (clockwise) out of the ecliptic plane. The angular width (2α) between the legs of the GCS model is 34° , 64° , and 36° for CME1, CME2, and CME3, respectively. These values are in agreement (within $\pm 10\%$) with the values obtained by Temmer et al. (2014). It is to be noted that the measured 2D angular width of a CME depends on the orientation of the GCS flux ropes. For ecliptic orientation of the flux ropes, i.e., $\gamma = 0^\circ$, the angular width of CME seen in 2D images is equal to the 3D edge-on angular width ($\omega_{EO} = 2\delta$) of the GCS model, where $\delta = \arcsin(\kappa)$. For $\gamma = 90^\circ$, the measured 2D width is equal to the 3D face-on angular width ($\omega_{FO} = 2\alpha + 2\delta$) of the GCS modeled CME.

We converted the GCS modeled 3D width to 2D angular width for CME2 using the expression $\omega_{2D} = \omega_{EO}\cos(\gamma) + \omega_{FO}\sin(\gamma)$, and find that CME2 has an approximately constant 2D angular width in COR2 FOV. We find that the fast CME3 has $\gamma = 21^\circ$, $\kappa = 0.40$, and $\alpha = 16^\circ$ in the beginning of the

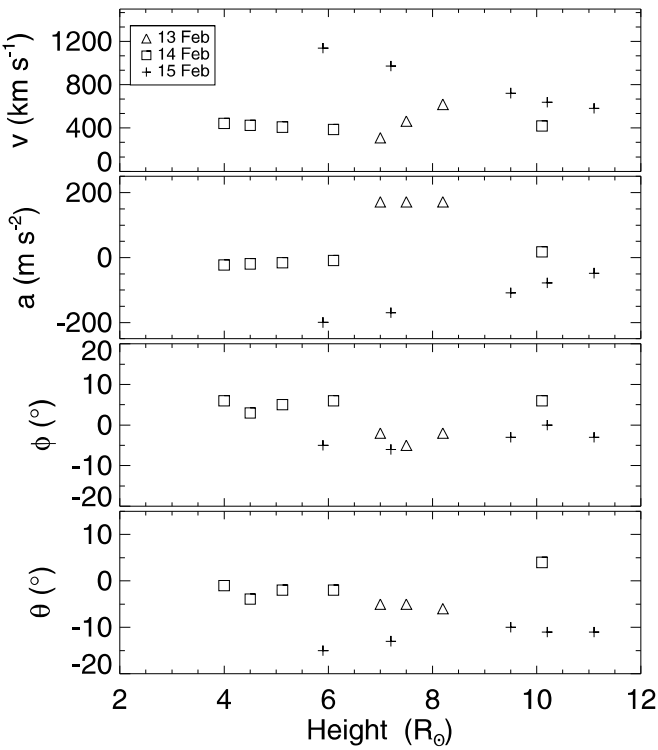


Figure 6. Top to bottom panels show the variations of radial velocity, acceleration, longitude, and latitude of CME1, CME2, and CME3 with radial height from the Sun.

COR2 FOV while it has $\gamma = 21^\circ$, $\kappa = 0.31$, and $\alpha = 18^\circ$ at the last measured point in COR2 FOV. Hence, we find that as CME3 propagates further in COR2 FOV, its 2D angular width (derived using the GCS modeled 3D width) decreases from 77° to 63° . These findings are in accordance with the observed 2D angular width of CME2 and CME3 (Figure 2). The possibility of rotation of CMEs has been discussed theoretically (Lynch et al. 2009, and references therein) and has been reported in low corona observations (Lynch et al. 2010). Such changes in the 2D measured angular width is also possible due to rotation (change in CME orientation, i.e., tilt, angle) of fast CME toward or away from the equator as shown by Yurchyshyn et al. (2009) who suggest higher rotation rate for a faster CME (Lynch et al. 2010; Poomvises et al. 2010). However, we emphasize that based on the GCS modeling, we could not infer any noticeable rotation (change in γ) or deflection (change in ϕ in Figure 6) in the COR2 FOV for the selected CMEs. The uncertainties involved in the estimation of 3D and observed 2D angular widths are discussed in Section 4.

Vourlidas et al. (2011) reported that despite the rapid rotation of CMEs there is no significant projection effects (change in angular width) in any single coronagraphic observations. They showed that the projected (2D) angular width of a CME is altered by only 10° between 2 to $15 R_\odot$ while a CME rotated by 60° over the same height range. We acknowledge the error in the measurements of tilt angle in our study, but it must be noted that a rotation of $\approx 40^\circ$ within 6 hr is required for the observed large variations in the 2D angular width of CME3, which is indeed not found in our analysis. Therefore, we consider that an observed decrease in the angular width of CME3 is not because of its rotation, but may be due to its interaction with solar wind or dense material from the preceding CME2.

2.2.3. Reconstruction of CMEs in HI FOV

Based on the kinematics observed close to the Sun, i.e., using COR observations, we consider the possibility that these Earth-directed CMEs have a chance of interaction and therefore we estimated their kinematics in HI FOV. We used the long-term background subtracted Level 2 data for HI observations taken from UKSSDC (<http://www.ukssdc.ac.uk/solar/stereo/data.html>). We examined the base difference images in HI FOV to notice any density depletion or enhancement due to the CME. Prior to this step, the HI image pair was aligned to remove the stellar contribution in the difference images. Furthermore, we notice that CME3 approached and met CME2 in the HI1 FOV. In this collision, the leading edge of CME3 flattened significantly. This observation motivated us to investigate the pre- and post-collision kinematics of CMEs, since in HI FOV, CMEs become faint and the tracking of the features out to larger distances invokes the uncertainties. Therefore, we track CMEs in the heliosphere by constructing the time-elongation map (*J*-map) (Davies et al. 2009), originally developed by Sheeley et al. (1999) and as described in detail in Section 3.1.1 of Mishra & Srivastava (2013).

The constructed *J*-map in the ecliptic plane for these CMEs in HI-A and -B FOV are shown in Figure 7. By tracking the bright leading fronts manually, we derive the elongation-time profiles for all three CMEs. In this figure, the derived elongation for the outward moving CMEs is overplotted with dotted color lines. The CME1 is very faint and could be tracked out to $\approx 13^\circ$ in the *STEREO-A* and *B* *J*-maps. However, CME2 and CME3 could be tracked out to 44° and 46° in *STEREO-A* *J*-maps, respectively, and out to $\approx 42^\circ$ in *STEREO-B* *J*-maps. The *J*-maps also show that the bright tracks of CME2 and CME3 approach close to each other, suggesting their possible collision in HI FOV.

Various stereoscopic reconstruction methods have been developed to estimate the kinematics of CMEs using SECCHI/HI images (Liu et al. 2010a; Lugaz et al. 2010; Davies et al. 2013). The selected CMEs in our study have a cone angular width of $\approx 60^\circ$; therefore, it is preferable to use those reconstruction methods that take into account the geometry of CMEs with similar angular width. Keeping these points in mind, we implemented the stereoscopic self-similar expansion (SSSE; Davies et al. 2013) method on the derived time-elongation profiles for all three CMEs to estimate their kinematics. While applying this method, we fixed the CME's cross-sectional angular half-width subtended at the Sun equal to 30° . Using the SSSE method for all three CMEs, the kinematics, i.e., estimated height, direction, and speed, were obtained (Figure 8). The speed was derived from the adjacent distance points using numerical differentiation with three-point Lagrange interpolation and therefore have systematic fluctuations. Estimating the speed in this way can provide short time variations in CME speed during its interaction with solar wind or other plasma density structures in the solar wind. On the other hand, the smoothed speed can also be derived if the estimated distance is fitted overall into an appropriate polynomial, but the information about variations of speed will be lost. Also, by fitting a polynomial for the derived fluctuating speeds, the speed can be shown with minimal fluctuations. Therefore, we have made a compromise and fitted the estimated distance during each five-hour interval into a first-order polynomial and derived the speed, which is shown with horizontal solid lines in the bottom panel of Figure 8. The error bars for the estimated parameters are also shown in this figure with vertical solid lines at each data point. The detailed procedure of the estimation of error bars is described in Section 2.2.4.

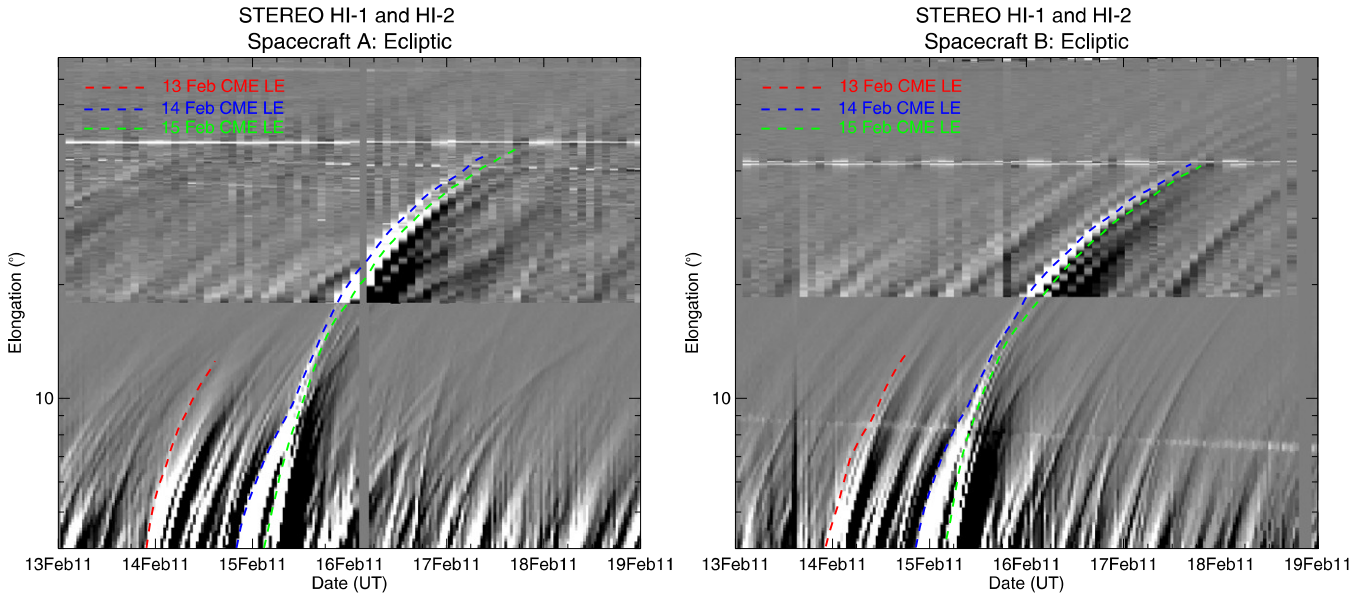


Figure 7. Time-elongation maps (J -maps) for *STEREO-A* (left) and *B* (right) using running differences of the images HI1 and HI2 are shown for the interval of 2011 February 13–19. The tracks of CME1, CME2, and CME3 are shown with red, blue, and green, respectively.

(A color version of this figure is available in the online journal.)

The propagation direction of CME2 and CME3 seem to follow the same trajectory and are approximately Earth directed. However, the unexpected variations in the direction of propagation of both CMEs were noticed, which is discussed in Section 4. In Figure 8, we noticed a jump in the speed of CME2 and CME3 at 08:25 UT on 2011 February 15. Within 18 hr, after an increase in speed is observed, the speed of the CME2 increases from about 300 km s^{-1} to 600 km s^{-1} . During this time the speed of CME3 decreased from about 525 km s^{-1} to 400 km s^{-1} . Later, both CMEs achieved a similar speed of $\approx 500 \text{ km s}^{-1}$. Such a finding of the acceleration of one CME and the deceleration of another, supports a possible collision between CME2 and CME3. The collision phase is shown in the top and bottom panels of Figure 8 (region between the two dashed vertical lines, from the left). After the collision, we find that both CMEs move in close contact with each other.

The strong deceleration of CME3 observed prior to the merging of the bright tracks (enhanced density front of CMEs) in J -maps, suggests possible interaction of CME3 with CME2. This is possible as we track the leading front of the CMEs using J -maps. The trailing edge of CME2 can cause an obstacle for the CME3 leading front, much earlier depending on its spatial scale. From the observed timings, it is clear that the interaction of CME3 with CME2 had started ≈ 5 hr prior to their collision in HI FOV. Our analysis also shows that the leading front of CME3 reflects the effect of interaction (i.e., strong deceleration) at $6 R_\odot$ while the leading edge of CME2 shows this effect (i.e., acceleration) at $28 R_\odot$. Therefore, the force acting on the trailing edge of CME2 takes approximately ≈ 5.7 hr to reach the leading front of this CME. Based on these values, the propagation speed of disturbance responsible for the acceleration of the leading front of CME2 should be $\approx 750 \text{ km s}^{-1}$. From the Radio and Plasma Wave Experiment (WAVES; Bougeret et al. 1995) on board the *WIND* spacecraft, we noticed a type II burst during 02:10–7:00 UT in the 16000–400 KHz range. Such radio bursts provide information on the CME-driven shock (Gopalswamy et al. 2000). This shock is associated with the fast CME3. The average shock cone angle ($\approx 100^\circ$) as seen from the Sun is

significantly greater than the average angular size ($\approx 45^\circ$) of any CME (Schwenn 2006). It is likely that this shock traveled across CME2. Therefore, the acceleration of CME2, observed in HI FOV, may be due to the combined effect of the shock and the leading front of CME3. As previously mentioned, CME1 was very faint, and its kinematics could be estimated up to $46 R_\odot$ only. Based on the linear extrapolation of the height–time curve of CME1 and CME2, we infer that they should meet each other at $144 R_\odot$ at 01:40 UT on 2011 February 17.

2.2.4. Comparison of Kinematics Derived from Other Stereoscopic Methods

To examine the range of uncertainties in the estimated kinematics of the CMEs of 2011 February 13–15, by implementing SSSE method, we applied another stereoscopic reconstruction method, viz. Tangent to a sphere (TAS; Lugaz et al. 2010) method to all three CMEs. Based on the estimated kinematics, we infer similar acceleration of CME2 and deceleration of CME3, as obtained by implementing SSSE method. Using TAS method, we found that the leading edge of CME3 caught the leading edge of CME2 at $26 R_\odot$ at 08:24 UT on February 15. Based on linear extrapolation of the height–time profile of CME2 and CME1, we inferred that CME2 would have reached CME1 at $157 R_\odot$ at 03:35 UT on 2011 February 17. We also implemented the Geometric Triangulation (GT; Liu et al. 2010a) method using the derived elongation–time profiles of tracked features of these CMEs to estimate their kinematics. On using GT method, we find similar results as obtained from TAS and SSSE methods. Based on the estimated kinematics from GT method, we note that the leading edge of CME3 caught the leading edge of CME2 at $24 R_\odot$ at 07:10 UT on February 15. The linear extrapolation of height–time for CME1 and CME2 suggest their interaction at $138 R_\odot$ on 20:24 UT on February 17.

The kinematics derived from SSSE method is shown in Figure 8 and cognizance of the involved uncertainties is important. However, the actual uncertainties in the derived kinematics owe to several factors (geometry, elongation measurements, Thomson scattering, line of sight integration effect, breakdown

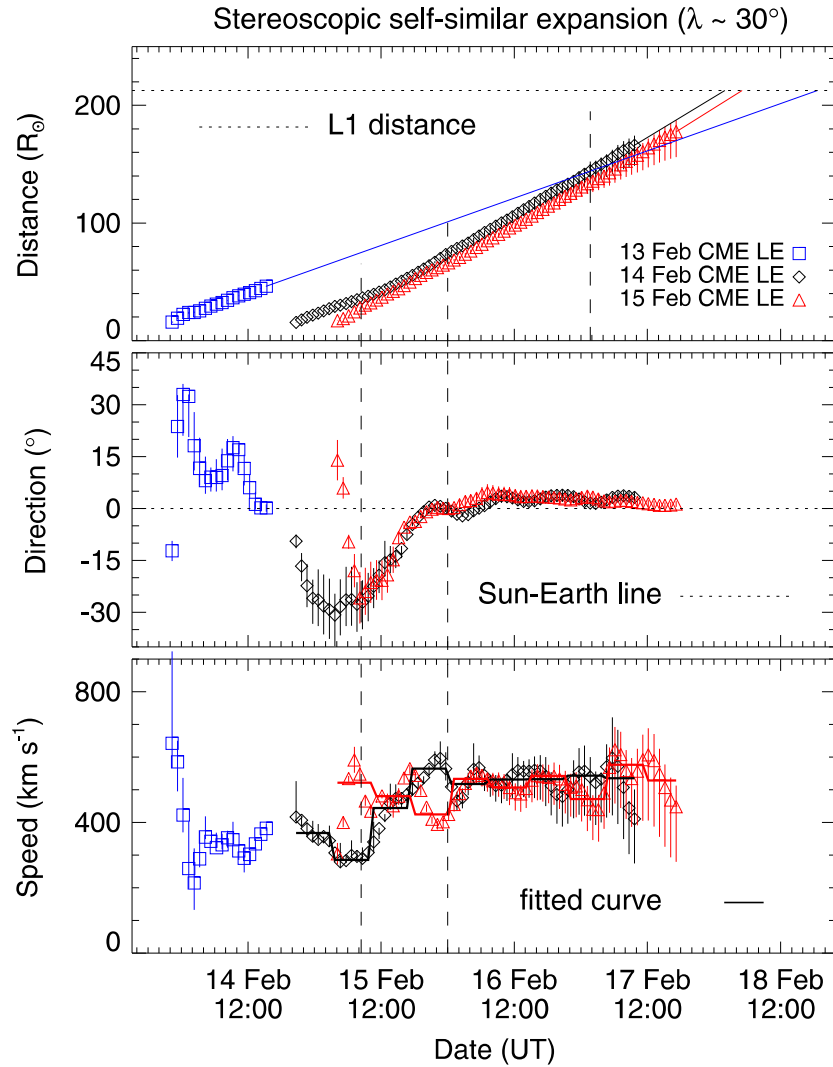


Figure 8. From top to bottom, distance, propagation direction, and speed (as obtained using SSSE method) of CME1 (blue), CME2 (black), and CME3 (red) are shown. In the top panel, the horizontal dashed line marks the heliocentric distance of the L1 point. In the middle panel, the dashed horizontal line marks the Sun–Earth line. In the bottom panel, speeds shown with symbols are estimated from differentiation of adjacent distances points using three-point Lagrange interpolation. The speed shown with the solid line is determined by differentiating the fitted first-order polynomial for estimated distance for each five-hour interval. From the left, the first and second vertical dashed lines mark the start and end of the collision phase of CME3 and CME2. In the top panel, the rightmost vertical dashed line marks the inferred interaction between CME2 and CME1. The vertical solid lines at each data point shows the error bars, explained in Section 2.2.4.

(A color version of this figure is available in the online journal.)

of assumptions in the method itself) and its quantification is extremely difficult. Davies et al. (2013) have shown that GT and TAS methods are special cases of SSSE method corresponding to two extreme cross-sectional extent (geometry) of CME, i.e., corresponding to angular half width of $\lambda = 0^{\circ}$ and $\lambda = 90^{\circ}$, respectively. We estimated the uncertainties due to consideration of different geometry in each of the three implemented stereoscopic techniques (GT, TAS and SSSE). Such uncertainties are shown with error bars with vertical solid lines in Figure 8. We estimated the absolute difference between kinematics values derived from SSSE and GT method and display it as a vertical lower error (lower segment of error bars). Similarly, the absolute difference between kinematics values from SSSE method and TAS method is displayed as vertical upper error. From Figure 8, we notice that the results from all three methods are in reasonable agreement.

Further, we attempted to examine the contribution of errors in the kinematics due to limited accuracy in tracking (i.e., elongation measurements) of a selected feature. Follow-

ing the error analysis approach of Liu et al. (2010b), we consider an uncertainty of 10 pixels in elongation measurements from both *STEREO* viewpoints which correspond to elongation uncertainty of $0^{\circ}04$, $0^{\circ}2$ and $0^{\circ}7$ in COR2, HI1 and HI2 FOV, respectively. This leads to an uncertainty of 0.20 – $0.35 R_{\odot}$, 0.21 – $0.75 R_{\odot}$, and 0.19 – $0.74 R_{\odot}$ in the estimated distance for CME1, CME2, and CME3, respectively. Such small uncertainties in the distance is expected to result in error of less than $\approx 100 \text{ km s}^{-1}$ in speed. However, similar elongation uncertainty lead to crucially larger uncertainty in the estimated direction of propagation of CMEs when they are close to entrance of HI1 FOV, where singularity occurs. The occurrence of singularity is described in earlier studies (Liu et al. 2011; Mishra & Srivastava 2013; Mishra et al. 2014b). The estimated propagation direction of CMEs from GT method are shown in Figure 9 in which vertical lines at each data point show the uncertainty in the direction.

Based on the aforementioned error estimation for the selected CMEs in our study, we find that the uncertainties in the

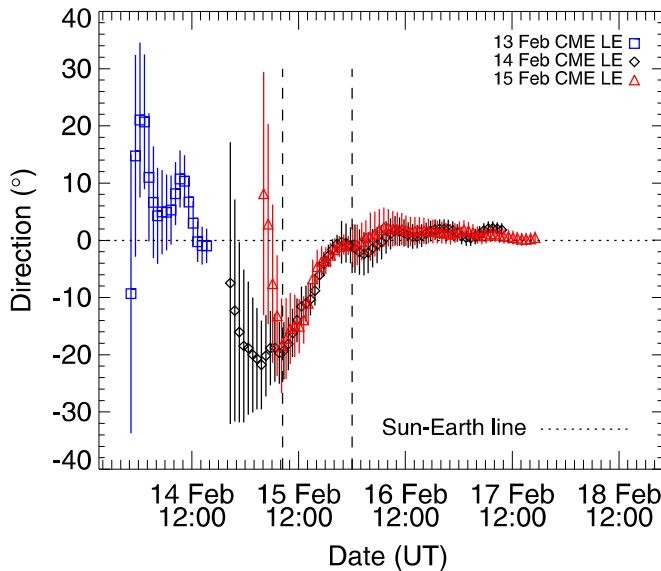


Figure 9. Estimates of direction for CME1 (blue), CME2 (black), and CME3 (red) from the GT method is shown. The vertical lines at each data point shows the error bars, which are calculated mathematically considering the uncertainties of 10 pixels in elongation measurements, i.e., in tracking the CMEs. The two vertical dashed lines mark the start and end of the collision phase of CME2 and CME3. The horizontal dashed line denotes the Sun–Earth line. The negative (positive) angle of direction stands for east (west).

(A color version of this figure is available in the online journal.)

estimated kinematics from stereoscopic methods owe mostly due to errors in elongation measurements rather than geometry. Due to the large separation between the two *STEREO* viewpoints and consequently occurrence of singularity, small observational errors in the elongation measurements yield significantly larger errors in the kinematics (especially in the direction), irrespective of the geometry considered for the CMEs (Davies et al. 2013; Mishra et al. 2014b).

2.3. Energy, Momentum Exchange, and Nature of Collision between CME2 and CME3

The dynamics and structure of CMEs are likely to change when they collide with one another; therefore, estimation of post-collision kinematics is essential to achieve the goal of space weather prediction. As the CMEs are large-scale magnetized plasmoids that interact with each other, it is worth investigating the nature of collision for CMEs, which is expected to be different than the collision of gaseous bubbles with no internal magnetic field. In collision dynamics, the total momentum of colliding bodies is conserved irrespective of the nature of collision, provided that external forces are absent.

We attempt to investigate the nature of collision for CME2 and CME3. As the CME3 follows the trajectory of CME2 before and also after the collision, we simply use the velocity derived from the SSSE method to deal with the collision dynamics. Therefore, we did not take into account the 3D velocity components and intricate mathematics for determining the motion of the centroid of colliding CMEs, as used in Shen et al. (2012). We studied 1D collision dynamics, which is similar to the case of a head-on collision for the interacting CMEs. We note that the start of the collision phase (marked by the dashed vertical line) occurs at the instant when the speed of CME2 started to increase while the speed of CME3 started to decrease (Figure 8, bottom panel). The same trend of speeds for both CMEs are maintained up to 18 hr where the collision phase ends. After

the end stage of the collision phase, CME2 and CME3 show a trend of deceleration and acceleration, respectively, toward a constant speed of 500 km s^{-1} . From the obtained velocity profiles (Figure 8), we notice that the velocity of CME2 and CME3 before the collision are $u_1 = 300$ and $u_2 = 525 \text{ km s}^{-1}$, respectively. After the collision and exchange of velocity, the velocity of CME2 and CME3 is found to be $v_1 = 600$ and $v_2 = 400 \text{ km s}^{-1}$, respectively. If the true mass of CME2 and CME3 is m_1 and m_2 , respectively, then the conservation of momentum requires $m_1 u_1 + m_2 u_2 = m_1 v_1 + m_2 v_2$. To examine the momentum conservation for the case of colliding CMEs, we need to calculate the true mass of both CMEs, which is discussed in the following section.

2.3.1. Estimation of the True Mass of CMEs

Historically, the mass of a CME has been calculated using the POS approximation, which resulted in an underestimated value (Munro et al. 1979; Poland et al. 1981; Vourlidas et al. 2000). We implemented the approach of Colaninno & Vourlidas (2009) and derived the true propagation direction and then the true mass of CMEs in COR2 FOV. Before applying this approach, base difference images were obtained following the procedure described in Vourlidas et al. (2000, 2010), Bein et al. (2013). To estimate the projected mass of CMEs in base difference COR2-A and B images, we selected a region of interest (ROI) that encompassed the full extent of a CME. The intensity at each pixel was then converted to the number of electrons at each pixel and then the mass per pixel was obtained. The total mass of the CME was calculated by summing the mass at each pixel inside this ROI. In this way, we estimated the projected mass of the CME, M_A and M_B , from the two viewpoints of *STEREO-A* and *B* in COR2 FOV.

According to Colaninno & Vourlidas (2009), CME mass M_A and M_B are expected to be equal to the same CME volume observed from two different angles. Any difference between these two masses must be due to the incorrect use of the propagation angle in the Thomson scattering calculation. Based on this assumption, they derived an equation for true mass (M_T) as a function of projected mass and true direction of propagation of the CME (see their Equations (7) and (8)). We used a slightly different approach to solve these equations:

$$M_A/M_B = B_e(\theta_A)/B_e(\theta_A + \Delta), \quad (1)$$

where θ_A is the angle of direction of propagation of CME measured from the POS of *STEREO-A*, $B_e(\theta_A)$ is the brightness of a single electron at an angular distance of θ_A from the POS, and Δ is the summation of longitude of both *STEREO-A* and *STEREO-B* from the Sun–Earth line. Once we obtained the measured values of M_A and M_B , we derive its ratio and calculate θ_A . In this way, we obtained multiple values of θ_A , which result in same value of the ratio of M_A and M_B . The correct value of θ_A was found by visual inspection of CME images in the COR FOV. Once we obtained the θ_A , the true mass of CME was estimated using Equation (4) of Colaninno & Vourlidas (2009). Here we must emphasize that the estimation of the true propagation direction of the CMEs (θ_A) using the aforementioned approach has large errors if the value of Δ approaches 180° . This is a severe limitation of the method of true mass estimation and arises because in such a scenario a CME from the Sun, despite its propagation in any direction (not only toward the Earth), will be measured at an equal propagation angle from the POS of both spacecraft. Therefore, in principle both the estimated

M_A and M_B should be exactly equal and any deviation (which is likely) will result in a highly erroneous value of θ_A , and consequently in the true mass of the CME. Such a limitation has also been reported by Colaninno & Vourlidas (2009) for a very small spacecraft separation angle. This implies that an accurate propagation direction cannot be derived with this method unless we adjust the separation angle between the *STEREO* spacecraft slightly. Hence, we use a slightly different value of $\Delta \approx 160^\circ$ for our case. By repeating our analysis several times for these CMEs, we noted that such a small change in Δ has a negligibly small effect on the CME mass. In our study, we have also determined the true mass using the 3D propagation direction obtained from another method (GCS forward fitting model) and found that these results are within $\approx 15\%$ of the mass estimates from the method of Colaninno & Vourlidas (2009).

In the present work, we have estimated the true masses of CME2 and CME3 to understand their collision phase. For CME2 at a heliocentric distance of $\approx 10 R_\odot$, M_A and M_B were estimated as 5.30×10^{12} kg and 4.38×10^{12} kg, respectively, and its propagation direction as 24° east from the Sun–Earth line. For CME3 at $\approx 12 R_\odot$, M_A and M_B were estimated as 4.56×10^{12} kg and 4.77×10^{12} kg, respectively, and its propagation direction as 30° east from the Sun–Earth line. The true mass of CME2 and CME3 is estimated as $m_1 = 5.40 \times 10^{12}$ kg and $m_2 = 4.78 \times 10^{12}$ kg, respectively. We also noticed that mass of CMEs increased with distance from the Sun and we interpret such an increase in mass as an observational artifact due to the emergence of CME material from behind the occulter of the coronagraphs; however, the possibility of a small real increase in CME mass cannot be ignored completely.

2.3.2. Estimation of Coefficient of Restitution

As per our calculations, the masses of the CMEs were found to become constant after $\approx 10 R_\odot$; therefore, we assume that these masses remain constant before and after their collision in HI FOV. Combining the equation of conservation of momentum with the equation of coefficient of restitution, the velocities of CME2 and CME3 after the collision can be estimated theoretically ($v_{1\text{th}}, v_{2\text{th}}$):

$$\begin{aligned} v_{1\text{th}} &= \frac{m_1 u_1 + m_2 u_2 + m_2 e(u_2 - u_1)}{(m_1 + m_2)}; \\ v_{2\text{th}} &= \frac{m_1 u_1 + m_2 u_2 + m_1 e(u_1 - u_2)}{(m_1 + m_2)}, \end{aligned} \quad (2)$$

where e is the coefficient of restitution, $e = v_2 - v_1/u_1 - u_2$ and signifies the nature of collision.

Using the velocity $(u_1, u_2) = (300, 525)$ km s $^{-1}$ and true mass values $(m_1, m_2) = (5.40 \times 10^{12}, 4.78 \times 10^{12})$ kg, we calculate a set of theoretical values of final velocity $(v_{1\text{th}}, v_{2\text{th}})$ after the collision of CMEs from Equation (2) corresponding to a set of different values of the coefficient of restitution (e). We define a parameter called variance, $\sigma = \sqrt{(v_{1\text{th}} - v_1)^2 + (v_{2\text{th}} - v_2)^2}$. Considering the theoretically estimated final velocity from Equation (2) and variance (σ) values, one can obtain the most suitable value of e corresponding to which the theoretically estimated final velocity $(v_{1\text{th}}, v_{2\text{th}})$ is found to be closest to the observed final velocity (v_1, v_2) of the CMEs. This implies that the computed variance is minimum at this e value.

We have estimated that the total kinetic energy of the system before the collision is 9.01×10^{23} joules. The individual

kinetic energy of CME2 and CME3 is 2.43×10^{23} joules and 6.58×10^{23} joules, respectively. We note that the momentum of CME2 and CME3 is 1.6×10^{18} N s and 2.5×10^{18} N s, respectively, just before their observed collision. Hence, the total momentum of the system is equal to 4.13×10^{18} N s. We consider (v_1, v_2) the estimated final velocity (from SSSE method) to be $(600, 400)$ km s $^{-1}$ (Figure 8). We found that $(v_{1\text{th}}, v_{2\text{th}}) = (495, 304)$ km s $^{-1}$ and the minimum value of σ is 142 corresponding to $e = 0.85$. For this value of e , the momentum is found to be conserved and the nature of the collision is found to be in the inelastic regime. Such a collision resulted in a decrease of total kinetic energy of the system by 2% of its value before the collision. If the coefficient of restitution is calculated by directly using the measured values of velocity, then e is estimated as 0.89, which is approximately equal to what is calculated from using the aforementioned theoretical approach.

To account for uncertainties in the results, we repeated our computation by taking an uncertainty of ± 100 km s $^{-1}$ in the estimated final velocity after the collision of CMEs. For example, if we use $(v_1, v_2) = (700, 500)$, then the minimum value of $\sigma = 288$ is found corresponding to $e = 0.80$. The estimate for σ is found to be minimum and is equal to 2.0, corresponding to $e = 0.90$, when $(v_1, v_2) = (500, 300)$ km s $^{-1}$ is used and in this case $(v_{1\text{th}}, v_{2\text{th}}) = (501, 298)$ is obtained. This means that keeping the conservation of momentum as a necessary condition, the combination of $(u_1, u_2) = (300, 525)$ km s $^{-1}$ and $(v_1, v_2) = (500, 300)$ km s $^{-1}$ with $e = 0.90$ best suits the observed case of the collision of CME2 and CME3. In this case, the total kinetic energy after the collision decreased by only 1.3%, the kinetic energy of CME2 increased by 177%, and the kinetic energy of CME3 decreased by 67% of its value before the collision. This implies that the observed collision is in the inelastic regime but closer to the elastic regime. For this case, the momentum of CME2 increased by 68% and the momentum of CME3 decreased by 35% of its value before their collision. Our analysis therefore shows that there is a huge transfer of momentum and kinetic energy during the collision phase of CMEs.

It is worth checking the effect of uncertainty in mass in the estimation of the value of e and hence on the estimation of the nature of the collision. We have estimated the true mass, which is also uncertain and difficult to quantify (Colaninno & Vourlidas 2009). However, a straightforward uncertainty arises from the assumption that CME structure lies in the plane of the 3D propagation direction of CME. Vourlidas et al. (2000) have shown that such a simplified assumption can cause the underestimation of CME mass by up to 15%. Applying this error to the estimated true mass of CME2 and CME3, their mass ratio ($m_1/m_2 = 1.12$) can range between 0.97 and 1.28. To examine the effect of larger uncertainties in the mass, we arbitrarily change the mass ratio between 0.5 to 3.0 in steps of 0.25 and repeat the aforementioned analysis (using Equation (2), and calculate the σ value) to estimate the value of e corresponding to each mass ratio. The variation of e with mass ratio is shown in Figure 10 corresponding to the observed final velocity $(v_1, v_2) = (600, 400)$ km s $^{-1}$ after the collision of the CMEs in our case. We have shown earlier that best suited final velocity of CMEs for our observed case of collision is $(v_1, v_2) = (500, 300)$ km s $^{-1}$; therefore, corresponding to this velocity, the variation of e with mass ratio is shown (Figure 10). In this figure, we have also plotted the estimated minimum variance corresponding to each obtained value of e . From this figure, it is evident that even if a large arbitrary mass ratio is considered,

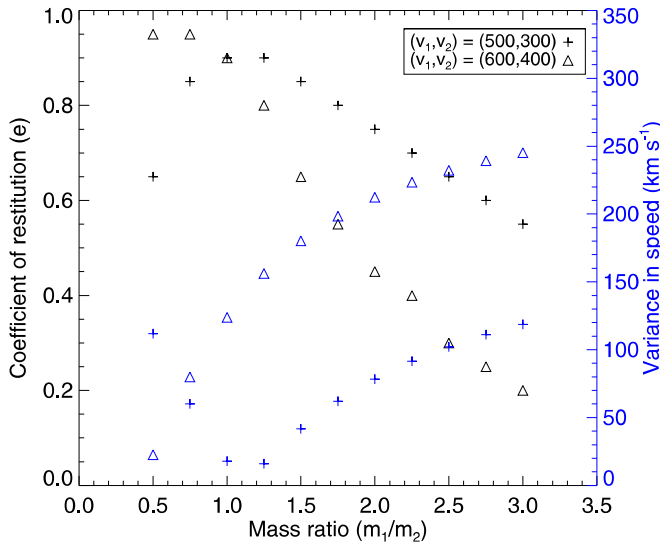


Figure 10. Best-suited coefficient of restitution values corresponding to different mass ratios of CME2 and CME3 are shown for their observed velocity in the post-collision phase (in black). We also show the variance in speed corresponding to the estimated best-suited coefficient of restitution (in blue). (A color version of this figure is available in the online journal.)

the nature of the collision remains in the inelastic regime. It never reaches a completely inelastic ($e = 0$), elastic ($e = 1$), or super-elastic ($e > 1$) regime.

3. IN SITU OBSERVATIONS, ARRIVAL TIME, AND GEOMAGNETIC RESPONSE OF THE INTERACTING CMEs

3.1. In Situ Observations

We analyzed the *WIND* spacecraft plasma and magnetic field observations taken from CDAWeb (<http://cdaweb.gsfc.nasa.gov/>). We attempted to identify the CMEs based on the criterion of Zurbuchen & Richardson (2006). The variations in plasma and magnetic field parameters from 2011 February 17 at 20:00 UT to February 20 at 04:00 UT are shown in Figure 11. The findings from in situ data analysis in our study are very similar to those reported by Marićić et al. (2014). Since we associate the remote observations to in situ observations and compare the arrival time of interacted CMEs, for sake of completeness we briefly discuss in situ observations. In Figure 11, the region marked R1, R2, and R3 is associated with CME1, CME2, and CME3, respectively. In region R3, the latitude and longitude of the magnetic field vector (from top, sixth and seventh panel of Figure 11) seemed to rotate and plasma beta (β) was found to be less than one. Therefore, this region (R3) may be termed a magnetic cloud (MC).

The region bounded between 09:52 UT and 10:37 UT on February 18 with the third and fourth dashed lines, from the left, shows a sharp decrease in magnetic field strength, enhanced temperature and flow speed, and a sudden change in longitude of the magnetic field vector. This region lasted for less than an hour, but represents a separate structure between R1 and R2, which could be a magnetic reconnection signature between field lines of region R1 and R2 (Wang et al. 2003; Gosling et al. 2005); however, an in-depth analysis is required to confirm this. In situ observations also reveal that region R2 is overheated $\approx 10^6$ K because it is squeezed between regions R1 and R3. Region R2 shows a high speed of 750 km s^{-1} at the front

while a very low speed of 450 km s^{-1} at its trailing edge. Such observations may indicate an extremely fast expansion of R2 due to magnetic reconnection at its front edge as suggested by Marićić et al. (2014). From an overall inspection of in situ data, it is clear that in situ measured plasma is heated ($\approx 10^5$ K for regions R1 and R3 and $\approx 10^6$ K for region R2) than what is observed ($\approx 10^4$ K) in general, in CMEs. Such signatures of compression and heating due to CME–CME interaction and passage of CME-driven shock through the preceding CME have also been reported in earlier studies (Lugaz et al. 2005; Liu et al. 2012; Temmer et al. 2012; Mishra et al. 2014a). From the in situ data, it is also noted that the spatial scale of CME1 (R1) and CME2 (R2) is smaller than CME3 (R3) and it may be possible due to their compression by the following CME or shock for each.

3.2. Estimation of Arrival Time of CMEs

If the measured 3D speeds (Figure 6) of CME2 and CME3 at the final height is assumed to be constant for the distance beyond COR2 FOV, then CME3 would have caught the CME2 at $39 R_\odot$ on 2011 February 15 at 17:00 UT. However, our analysis of HI observations (using *J*-maps) shows that these two CMEs collided ≈ 7 hr earlier (at $\approx 28 R_\odot$). This could have happened for several reasons: first, because the COR and HI observations tracked two different features. Second, a deceleration of CME2 beyond COR2 FOV may also be partially responsible for this. Taking 3D speed estimated in COR2 FOV as a constant up to L1, the arrival times of CME1, CME2, and CME3 at L1 will be at 13:00 UT on February 16, at 20:10 UT on February 18, and 23:20 UT on February 17, respectively. However, as discussed in Section 2.2.3, after the collision between CME2 and CME3, the dynamics of the CMEs changed. Therefore, we extrapolated linearly the height–time plot up to L1 by taking the few last points in the post-collision phase of these CMEs and we obtained their arrival time. Such extrapolation may contribute to uncertainties in the arrival times of CMEs (Colaninno et al. 2013). From these extrapolations (shown in the top panel of Figure 8), the obtained arrival time of CME2 and CME3 at L1 is on 2011 February 18 at 02:00 UT and 05:00 UT, respectively. These extrapolated arrival times for CME2 and CME3 are 12 hr earlier and 6 hr later, respectively, than estimated from measurements made in COR2 FOV. Based on these results, we infer that after the collision of CME2 and CME3, CME2 gained kinetic energy and momentum at the cost of the kinetic energy and momentum of CME3. The arrival time of CME3 is also estimated (within an error of 0.8 to 8.6 hr) by Colaninno et al. (2013) by applying the various fitting approaches to the deprojected height–time data derived by using the GCS model with the SECCHI images.

We associate the starting times of in situ structures marked as R1, R2, and R3 (in Figure 11) with the actual arrival of CME1, CME2, and CME3, respectively. We find that marked leading edge of CME1 at L1 is ≈ 14 hr earlier than that estimated by extrapolation. The extrapolated arrival time for CME1 is 18:40 UT on February 18. This difference can be explained by assuming a possible acceleration of CME1 beyond the tracked points in HI FOV. We have extrapolated CME1 height–time tracks from its pre-interaction phase because CME1 could not be tracked in *J*-maps up to longer elongations where the interaction is inferred. This highlights the possibility that after its interaction with a CME2- or CME3-driven shock (discussed in Section 2.2.3), CME1 has accelerated.

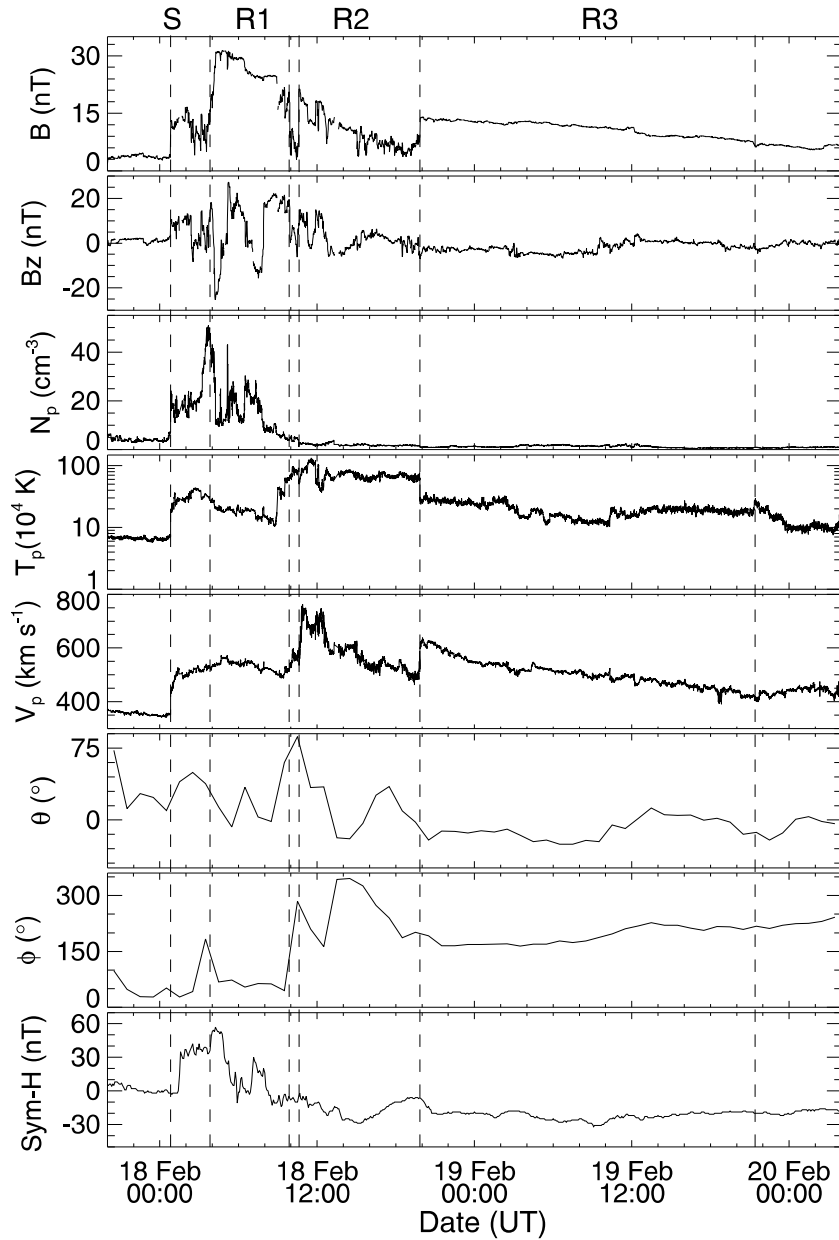


Figure 11. From top to bottom, panels show the variations of magnetic field strength, southward component of magnetic field, proton density, proton temperature, proton flow speed, latitude, longitude of magnetic field vector, and longitudinally symmetric disturbance index for horizontal (dipole) direction, respectively. From the left, first, second, third, fourth, fifth, and sixth vertical lines mark the arrival of the shock, leading edge of CME1, trailing edge of CME1, leading edge of CME2, trailing edge of CME2, and trailing edge of CME3. S, R1, R2, and R3 stand for the arrival of the shock and the bounded interval for CME1, CME2, and CME3 structures, respectively.

The actual arrival time of the CME2 and CME3 leading edge (shown in Figure 11) is ≈ 8.5 and 15 hr later, respectively, than obtained by direct linear extrapolation of height–time curve (Figure 8). From the aforementioned arrival time estimates, we notice an improvement in arrival time estimation of CME2 and CME3 by a few (up to 10) hours, when the post-collision speeds are used rather than their speeds before the collision. The average measured (actual) transit speed of CME2 and CME3 at L1 is approximately 100 km s^{-1} larger than its speed in remote observations in the post-collision phase. Such an inconsistency of delayed arrival even having larger speeds is possible only if it is assumed that CME2 and CME3 over-expand before reaching L1, or the in situ spacecraft is not hit by the nose of these CMEs (Marićić et al. 2014). The short duration of CME2 in the in situ data with a lack of magnetic cloud signature favors a flank

encounter of CME2 at the spacecraft. The late arrival of CME3 may also be due to its higher deceleration than estimated in HI FOV. Such inconsistency may also arise if the remotely tracked feature is incorrectly identified in the in situ data.

3.3. Geomagnetic Response of Interacting CMEs

In the bottom panel of Figure 11, the longitudinally symmetric disturbance (Sym-H) (Iyemori 1990) index is plotted. This index is similar to the hourly disturbance storm time (Dst) (Sugiura 1964) index but uses one-minute values recorded from a different set of stations and a slightly different coordinate system and method to determine the base values. The effect of solar wind dynamic pressure can be more clearly seen in the Sym-H index than in the hourly Dst index. We observed

a sudden increase in the Sym-H index up to 30 nT around 01:30 UT on February 1, 8 which is within an hour of the arrival of interplanetary shock. The Sym-H index continued to rise, and around 04:15 UT reached 57 nT. We noticed that the first steep rise in this index marked by the shock is represented by enhanced magnetic field, speed, and density. The second peak in Sym-H is primarily due to a corresponding peak in magnetic field strength and density, but no peak in speed was observed during this time. During the passage of region R1, the z-component of the IP magnetic field (B_z) began to turn negative at 04:07 UT and remained so up to one hour. During this period, its values reached down to -25 nT at 04:15 UT and then turned to positive values around 05:00 UT. We noticed that B_z turned negative a second time at 07:07 UT and remained so for 47 minutes, reaching a value of -15 nT at 07:31 UT on February 18. From the Sym-H plot, it is clear that these two negative turns of B_z caused a rapid decrease in elevated sym-H values. Dungey (1961) has shown that the negative B_z values and the process of magnetic reconnection at the magnetosphere enables magnetized plasma to transfer its energy into the magnetosphere and form a ring current.

Succinctly, we infer that the arrival of magnetized plasma can be attributed to the strong storm sudden commencement (SSC; $Dst = 57$ nT) and short-duration (47 minutes) negative B_z field therein resulted in a minor geomagnetic storm ($Dst = -32$ nT). It seems that the intensity of the SSC is independent of the peak value of depression in the horizontal component of the magnetic field during the main phase of a geomagnetic storm. Our analysis supports the idea of collision (or interaction) of multiple CMEs, which can enhance the magnetic field strength, density, and temperature within the CMEs (Liu et al. 2012; Möstl et al. 2012). Such enhanced parameters can increase the conductivity of the CME plasma and result in intense induced electric current in the CME when it propagates toward the Earth's magnetic field. This induced electric current within the CME plasma causes its intense shielding from Earth's field and increases the magnetic field intensity around the Earth, which is manifested as SSC (Chapman & Ferraro 1931).

4. RESULTS AND DISCUSSION

In what follows, we summarize our results of the analysis of the interaction of three Earth-directed CMEs launched in succession during 2011 February 13–15, focusing on three main aspects. These include the morphological study, the kinematic study of interacting CMEs, and then near-Earth manifestations.

4.1. Morphological Evolution of CMEs

We have studied the morphological properties of Earth-directed CMEs (CME2 and CME3) when the separation angle between *STEREO-A* and *STEREO-B* is 180° . On comparing the morphological evolution of the CMEs with the cone model, we found that the slow CME2 maintained a constant angular width in the corona, but the angular width of the fast CME3 decreased monotonically as it propagated further in the corona. The possible explanation for this is that when CME3 is launched from the Sun, its leading edge suddenly experiences the ambient solar wind pressure and the result is its flattening (Odstrcil et al. 2005), causing a large angular width. However, as CME3 propagates further in the corona, there is a decrease in interaction between the solar wind and the part of CME (i.e., near apex of the cone) that decides the angular width; therefore, a decrease in angular width is noticed away from the Sun.

The difference in the cone and contour area of CME2 increases linearly with the radial height of the CME leading edge (bottom panel of Figure 3). This can be explained by the fact that CME2 interacted with the solar wind such that its leading edge (specially the nose) stretched out, thereby increasing the value of r (distance between Sun-center and the nose of the CME) and also the ice-cream-cone area. For the fast CME3, we find that the contour area is less than the cone area close to the Sun, but as the CME propagated further in the corona, its contour area became larger than the cone area (Figure 4). This can be possibly explained by the concept that, contrary to the behavior of CME2, as the CME3 propagated further in the corona its front flattened due to drag force, leading to spilling some CME mass outside the cone, i.e., at the flanks of the CME. This flattening resulted in a lower estimated value of r and hence a decrease in the estimated cone area. Therefore, a negative value is obtained for the difference between the cone area and the contour area (bottom panel of Figure 4). From Figures 3 and 4 (bottom panels), we can say that slow and fast CMEs deviate differently from the cone model.

Our analysis shows that the estimated 2D angular width (converted from 3D) follows the same trend as observed in 2D images (Figure 2), but has a slightly different (within 5% for CME3 and 15% for CME2) value at a certain height. We also emphasize that the GCS model parameters (γ , κ and α) are very sensitive (Thernisien et al. 2009) and can only be fitted with limited accuracy, especially for a fast CME whose front gets distorted (see Figure 4) due to possible interaction with solar wind. Also, the estimation of these parameters depends on the visual agreement between a GCS-modeled CME and an observed CME, and is dependent on the user. We note that the minor error in these sensitive parameters can lead to significant errors in the 3D edge-on and face-on width of a GCS-modeled CME. This is the reason, despite reasonably good agreement between the GCS model parameters derived in our study with those derived in Temmer et al. (2014), the 3D values of angular widths for CME3 do not match well with their results. However, we acknowledge that measurements of the observed 2D width (Figure 2) also has some error (within 5°), which is quite small compared to the involved uncertainties in 3D or 2D angular width estimated from the GCS model. In light of the aforementioned uncertainties and results, further work needs to be carried out to investigate the change in angular width of fast CMEs.

4.2. Kinematic Evolution of Interacting CMEs

The 3D speed and direction estimated for three selected CMEs in COR2 FOV suggest their possible interaction in the IP medium. We have found that CME3 is the fastest among all three CMEs and shows strong deceleration in the COR2 FOV because of the preceding CME2, which acts as barrier for it. From the analysis of kinematics of CMEs in the heliosphere using stereoscopic methods, we have noted that a collision between CME3 and CME2 took place around $24 R_\odot$ – $28 R_\odot$. As the CME1 was faint and could not be tracked up to HI2 FOV in J -maps, we inferred based on the extrapolation of distances that CME2 caught up with CME1 between $138 R_\odot$ to $157 R_\odot$.

It may be noted that using three stereoscopic methods in our study, the estimates of velocity and location of collision for the three selected CMEs are approximately same (within a reasonable error of a few tens of km s^{-1} and within a few solar radii) as those obtained by Marićić et al. (2014) using a single spacecraft method. However, it is worth investigating the relative

importance of using single HI observations and simultaneous HI observations from the twin *STEREO* viewpoints for several CMEs launched in different directions at different *STEREO* spacecraft separation angles.

We have identified the signatures of collision of the CMEs in the kinematics profiles as exchange in their speed. We analyzed momentum and energy exchange during the collision phase of CME2 and CME3 and found that the nature of the collision was in an inelastic regime, reaching close to elastic. This is in contrast to the finding of Shen et al. (2012) who have reported a case of interacting CMEs in a super-elastic regime. Also, in another study we have found a case of collision of CMEs that was close to perfectly inelastic in nature (Mishra et al. 2014a). Therefore, it is worth investigating further what decides the nature of collision and which process is responsible for magnetic and thermal energy conversion to kinetic energy to make a collision super-elastic. Further in-depth study is required to examine the role of duration of the collision phase and impact velocity of CMEs for deciding the nature of collision.

The time variations of the estimated direction of propagation of CMEs (Figure 8) shows a surprisingly large change toward the sunward (entrance) edge of HI1 FOV. As explained in Section 2.2.4 these variations are not physical (real) and are mainly due to uncertainties in the measurements of elongation angles. We emphasize that in our analysis of collision dynamics of the CMEs, we do not expect large errors to switch in our results because the speed (derived from the distance) has smaller errors (as shown in Figure 8) in comparison to the direction. Moreover, the estimated uncertainties in the derived speed and direction are relatively smaller during the collision phase of the CMEs. Also, we have considered sufficiently large uncertainties in the mass and speed to estimate the nature of collision. Therefore, we advocate that the analysis carried out in this study is reliable.

The present analysis for collision dynamics may have small uncertainties due to the adopted boundary for the start and end of the collision phase. It is often difficult to define the start of the collision as the following CME (CME3) starts to decelerate (due to its interaction with the preceding CME) and the preceding CME (CME2) starts to accelerate before (most possibly due to a shock driven by the following CME) they actually merge as observed in HI FOV. Also, the assumption that there is no mass transfer between CME2 and CME3 during collision may result in some uncertainties. Furthermore, we have not taken into account the expansion velocity and propagation direction of the centroid of the CMEs, which may be different before and after the collision. In our study, we found that even after considering reasonable uncertainties in the derived mass and velocity parameters, the coefficient of restitution (e) lies between 0.78 to 0.90 for the interacting CME2 and CME3. This implies that the total kinetic energy of the system of CMEs after the collision is less than its value before the collision. In our analysis, we used the total mass of CMEs to study their collision dynamics, but as the CME is not a solid body, its total mass is not expected to participate in the collision. Keeping in mind various limitations of the present study, we believe that more detailed work, by incorporating various plasma processes, is required to understand the CME–CME interaction.

4.3. Interacting CMEs Near the Earth

We have examined the interaction and the collision signatures of CMEs in the in situ (*WIND*) observations. The interacting CMEs could be identified as a separate entity in the in situ

observations, therefore could not be termed as complex ejecta as defined by Burlaga et al. (2002). The in situ observations suggest that a shock launched by the fastest CME (CME3) passed through the CME2 and CME1 and caused compression, heating, and acceleration, in particular for CME2, which is sandwiched between the preceding CME (CME1) and the following CME (CME3). Our analysis shows that the interacting CMEs resulted in a minor geomagnetic storm with a strong long duration SSC. This is in contrast to the results of Farrugia & Berdichevsky (2004), Farrugia et al. (2006), and Mishra et al. (2014a), which suggested that interaction of CMEs leads to a long duration southward component of the magnetic field and therefore to strong geomagnetic storms.

We have found that using the kinematics derived from stereoscopic methods, in our study, the estimated arrival times of the CMEs are slightly (only by few hours) better than those of Marićić et al. (2014). This does not raise questions on the efficacy of stereoscopic reconstruction methods and long tracking of CMEs using *J*-maps, but it simply demonstrates that speeds determined from stereoscopic reconstruction methods and the single spacecraft HM method is approximately the same for the selected Earth-directed CMEs during the *STEREO* separation angle of 180°.

5. CONCLUSIONS

Based on our analysis of the interacting CMEs of 2011 February 13–15 by combining the wide angle imaging and in situ observations, we conclude the following.

1. The collision between CME2 and CME3 is observed at 24–28 R_{\odot} while the collision between CME1 and CME2 is inferred at 138–157 R_{\odot} . This highlights that heliospheric imaging is important for observing the collision of CMEs and estimating their post-collision dynamics.
2. We find that the observed collision of CME2 and CME3 is in an inelastic regime reaching close to elastic, whereas earlier studies have shown the nature of the collision of CMEs as super-elastic (Shen et al. 2012) and close to perfectly inelastic (Mishra et al. 2014a). Therefore, further investigations of interacting CMEs are required to understand the nature of collision.
3. The total kinetic energy of the CMEs after the observed collision is reduced by 1.3% of its value before the collision. The exchange of momentum between interacting CMEs ranges from 35% to 68% of its values before the collision.
4. The in situ measurements of these CMEs near 1 AU show that the preceding CME1 and CME2 are accelerated, compressed, and heated by overtaking CME3 and the shock driven by it.
5. Our results do not favor the possibility of the strengthening of the geomagnetic response as a consequence of the arrival of two or more interacting CMEs near the Earth. In fact, the interacting CMEs of February 13–15 lead to a minor geomagnetic storm ($Dst \approx -32$ nT), although a strong long duration SSC ($Dst \approx 57$ nT) is noticed. This finding is in contrast to earlier inferences by Farrugia & Berdichevsky (2004), Farrugia et al. (2006), Mishra et al. (2014a).
6. The morphological evolution of CMEs propagating with slow and fast, compared to ambient solar wind speed, seem to be different.

Our study of interacting CMEs highlights the importance of HI observations and their association with in situ observations to understand the nature of CME–CME interaction in detail and for

improved prediction of CME arrival time using post-interaction kinematics. We have also highlighted the difficulties inherent in reliably understanding the kinematics, arrival time, and nature of collision as well as the morphological evolution of CMEs.

The authors thank Jackie A. Davies and Manuela Temmer for their valuable comments and useful discussions. We acknowledge the team members of *STEREO* COR and HI as well as *WIND* instruments. We acknowledge the UK Solar System Data Center for providing the processed Level-2 *STEREO*/HI data. We also express our appreciation to the referee for insightful comments.

REFERENCES

- Bein, B. M., Temmer, M., Vourlidas, A., Veronig, A. M., & Utz, D. 2013, *ApJ*, **768**, 31
- Bougeret, J.-L., Kaiser, M. L., Kellogg, P. J., et al. 1995, *SSRv*, **71**, 231
- Brueckner, G. E., Howard, R. A., Koomen, M. J., et al. 1995, *SoPh*, **162**, 357
- Burlaga, L. F., Behannon, K. W., & Klein, L. W. 1987, *JGR*, **92**, 5725
- Burlaga, L. F., Plunkett, S. P., & St. Cyr, O. C. 2002, *JGR*, **107**, 1266
- Burlaga, L. F., Skoug, R. M., Smith, C. W., et al. 2001, *JGR*, **106**, 20957
- Chapman, S., & Ferraro, V. C. A. 1931, *TeMAE*, **36**, 171
- Colaninno, R. C., & Vourlidas, A. 2009, *ApJ*, **698**, 852
- Colaninno, R. C., Vourlidas, A., & Wu, C. C. 2013, *JGRA*, **118**, 6866
- Davies, J. A., Harrison, R. A., Rouillard, A. P., et al. 2009, *GeoRL*, **36**, 2102
- Davies, J. A., Perry, C. H., Trines, R. M. G. M., et al. 2013, *ApJ*, **776**, 1
- Dungey, J. W. 1961, *PhRvL*, **6**, 47
- Echer, E., Gonzalez, W. D., Tsurutani, B. T., & Gonzalez, A. L. C. 2008, *JGR*, **113**, 5221
- Eyles, C. J., Harrison, R. A., Davis, C. J., et al. 2009, *SoPh*, **254**, 387
- Farrugia, C., & Berdichevsky, D. 2004, *AnGeo*, **22**, 3679
- Farrugia, C. J., Jordanova, V. K., Thomsen, M. F., et al. 2006, *JGR*, **111**, 11104
- Fisher, R. R., & Munro, R. H. 1984, *ApJ*, **280**, 428
- Gopalswamy, N., Kaiser, M. L., Thompson, B. J., et al. 2000, *GeoRL*, **27**, 1427
- Gopalswamy, N., Yashiro, S., Kaiser, M. L., Howard, R. A., & Bougeret, J.-L. 2001, *JGR*, **106**, 29219
- Gopalswamy, N., Yashiro, S., Michałek, G., et al. 2002, *ApJL*, **572**, L103
- Gosling, J. T., Bame, S. J., McComas, D. J., & Phillips, J. L. 1990, *GeoRL*, **17**, 901
- Gosling, J. T., Skoug, R. M., McComas, D. J., & Smith, C. W. 2005, *JGR*, **110**, 1107
- Harrison, R. A., Davies, J. A., Möstl, C., et al. 2012, *ApJ*, **750**, 45
- Howard, R. A., Michels, D. J., Sheeley, N. R., Jr., & Koomen, M. J. 1982, *ApJL*, **263**, L101
- Howard, R. A., Moses, J. D., Vourlidas, A., et al. 2008, *SSRv*, **136**, 67
- Intriligator, D. S. 1976, *SSRv*, **19**, 629
- Iyemori, T. 1990, *JGG*, **42**, 1249
- Kaiser, M. L., Kucera, T. A., Davila, J. M., et al. 2008, *SSRv*, **136**, 5
- Liu, Y., Davies, J. A., Luhmann, J. G., et al. 2010a, *ApJL*, **710**, L82
- Liu, Y., Luhmann, J. G., Bale, S. D., & Lin, R. P. 2011, *ApJ*, **734**, 84
- Liu, Y., Thernisien, A., Luhmann, J. G., et al. 2010b, *ApJ*, **722**, 1762
- Liu, Y. D., Luhmann, J. G., Möstl, C., et al. 2012, *ApJL*, **746**, L15
- Lugaz, N. 2010, *SoPh*, **267**, 411
- Lugaz, N., Farrugia, C. J., Davies, J. A., et al. 2012, *ApJ*, **759**, 68
- Lugaz, N., Hernandez-Charpak, J. N., Roussev, I. I., et al. 2010, *ApJ*, **715**, 493
- Lugaz, N., Manchester, W. B., IV., & Gombosi, T. I. 2005, *ApJ*, **634**, 651
- Lugaz, N., Vourlidas, A., & Roussev, I. I. 2009, *AnGeo*, **27**, 3479
- Lynch, B. J., Antiochos, S. K., Li, Y., Luhmann, J. G., & DeVore, C. R. 2009, *ApJ*, **697**, 1918
- Lynch, B. J., Li, Y., Thernisien, A. F. R., et al. 2010, *JGRA*, **115**, 7106
- Marićić, D., Vršnak, B., Dumbović, M., et al. 2014, *SoPh*, **289**, 351
- Michalek, G., Gopalswamy, N., & Yashiro, S. 2003, *ApJ*, **584**, 472
- Mishra, W., & Srivastava, N. 2013, *ApJ*, **772**, 70
- Mishra, W., Srivastava, N., & Chakrabarty, D. 2014a, *SoPh*, in press (arXiv:1408.0352)
- Mishra, W., Srivastava, N., & Davies, J. A. 2014b, *ApJ*, **784**, 135
- Möstl, C., Farrugia, C. J., Kilpua, E. K. J., et al. 2012, *ApJ*, **758**, 10
- Munro, R. H., Gosling, J. T., Hildner, E., et al. 1979, *SoPh*, **61**, 201
- Odstrcil, D., Pizzo, V. J., & Arge, C. N. 2005, *JGRA*, **110**, 2106
- Odstrcil, D., Vandans, M., Pizzo, V. J., & MacNeice, P. 2003, in *AIP Conf. Ser.* **679**, *Solar Wind Ten*, ed. M. Velli, R. Bruno, F. Malara, & B. Bucci (Melville, NY: AIP), 699
- Poland, A. I., Howard, R. A., Koomen, M. J., Michels, D. J., & Sheeley, N. R., Jr. 1981, *SoPh*, **69**, 169
- Poomvises, W., Zhang, J., & Olmedo, O. 2010, *ApJL*, **717**, L159
- Schwenn, R. 2006, *LRSP*, **3**, 2
- Sheeley, N. R., Walters, J. H., Wang, Y.-M., & Howard, R. A. 1999, *JGR*, **104**, 24739
- Shen, C., Wang, Y., Wang, S., et al. 2012, *NatPh*, **8**, 923
- St. Cyr, O. C., Plunkett, S. P., Michels, D. J., et al. 2000, *JGR*, **105**, 18169
- Sugiura, M. 1964, *Ann. Int. Geophys.*, **35**, 49
- Temmer, M., Veronig, A. M., Kontar, E. P., Krucker, S., & Vršnak, B. 2010, *ApJ*, **712**, 1410
- Temmer, M., Veronig, A. M., Peinhart, V., & Vršnak, B. 2014, *ApJ*, **785**, 85
- Temmer, M., Veronig, A. M., Vršnak, B., et al. 2008, *ApJL*, **673**, L95
- Temmer, M., Vršnak, B., Rollett, T., et al. 2012, *ApJ*, **749**, 57
- Thernisien, A., Vourlidas, A., & Howard, R. A. 2009, *SoPh*, **256**, 111
- Vandas, M., Fischer, S., Dryer, M., et al. 1997, *JGR*, **102**, 22295
- Vourlidas, A., Colaninno, R., Nieves-Chinchilla, T., & Stenborg, G. 2011, *ApJL*, **733**, L23
- Vourlidas, A., Howard, R. A., Esfandiari, E., et al. 2010, *ApJ*, **722**, 1522
- Vourlidas, A., Subramanian, P., Dere, K. P., & Howard, R. A. 2000, *ApJ*, **534**, 456
- Vršnak, B., Žic, T., Falkenberg, T. V., et al. 2010, *A&A*, **512**, A43
- Vršnak, B., Žic, T., Vrbanec, D., et al. 2013, *SoPh*, **285**, 295
- Wang, Y. M., Ye, P. Z., & Wang, S. 2003, *JGRA*, **108**, 1370
- Williams, A. O., Davies, J. A., Milan, S. E., et al. 2009, *AnGeo*, **27**, 4359
- Xie, H., Ofman, L., & Lawrence, G. 2004, *JGR*, **109**, 3109
- Xue, X. H., Wang, C. B., & Dou, X. K. 2005, *JGR*, **110**, 8103
- Yurchyshyn, V., Abramenco, V., & Tripathi, D. 2009, *ApJ*, **705**, 426
- Zhao, X. P., Plunkett, S. P., & Liu, W. 2002, *JGR*, **107**, 1223
- Zurbuchen, T. H., & Richardson, I. G. 2006, *SSRv*, **123**, 31